Research Square

Preprints are preliminary reports that have not undergone peer review. They should not be considered conclusive, used to inform clinical practice, or referenced by the media as validated information.

Extreme temperature gradient drives substantial thermoelectric current in additive manufacturing

Fengyuan Lin
State Key Laboratory of Solidification Processing
Hui Chen
hchen1984@nwpu.edu.cn

State Key Laboratory of Solidification Processing
Yajing Sun
State Key Laboratory of Solidification Processing
Haiou Yang
State Key Laboratory of Solidification Processing
Meng Wang
State Key Laboratory of Solidification Processing
Wentao Yan
National University of Singapore
Xin Lin
State Key Laboratory of Solidification Processing

Article

Keywords:

Posted Date: October 23rd, 2026

DOI: https://doi.org/10.21203/rs.3.rs-11276543/v1

License: This work is licensed under a Creative Commons Attribution 4.0 International License.
Read Full License

Additional Declarations: No competing interests reported.

Extreme temperature gradient drives substantial thermoelectric current in additive manufacturing

Fengyuan Lin[1,+], Hui Chen[1,+,*], Yajing Sun[1], Haiou Yang[1], Meng Wang[1], Wentao Yan[2,*], Xin Lin[1,*]

[1] State Key Laboratory of Solidification Processing, Northwestern Polytechnical University, Xi'an 710072, China

[2] Department of Mechanical Engineering, National University of Singapore, Singapore, 117575, Singapore

Abstract Thermoelectric effects are commonly neglected in engineering alloys because their Seebeck coefficients are small. Here we show that this material-centred assumption fails under the extreme temperature gradients of additive manufacturing (AM). Combining in situ measurements of transient potential with multiphysics simulations under representative conditions of laser-powder-bed-fusion and laser-directed-energy-deposition. In our experiments we find that temperature gradients of ~10^5–10^8 K m^{-1} generate current densities of ~10^6–10^8 A m^{-2} in melt pool of AlSi10Mg, despite its Seebeck coefficient of only ~2 μV K^{-1}. These values match or exceed current densities in some conditions of thermoelectric materials. Additionally, we established a fully coupled thermoelectric magnetohydrodynamic (TEMHD) model that incorporates complete thermoelectric effects, and investigated the influence of thermoelectric source terms on the multi-physics coupling process. The currents are strongly anisotropic and spatially heterogeneous within

+ These authors contributed equally

*Corresponding authors: Hui Chen, hchen1984@nwpu.edu.cn; Wentao Yan, mpeyanw@nus.edu.sg; Xin Lin, xlin@nwpu.edu.cn

the melt pool. The resulting Joule and Thomson heat terms locally rival or exceed heat losses from the melt-pool surface, changing regional temperature gradients by ~1–10% and current densities by ~2–15%, whereas the Peltier term remains weak. Although the specific microstructural consequences remain to be established, the magnitude, localization and thermal feedback of thermoelectric currents identify them as an inherent non-negligible component of melt-pool dynamics and solidification in AM, and as a pre-existing electrical background for magnetically or electrically assisted process. Our high-fidelity TEMHD model provides an effective tool for studying this class of problems.

Thermoelectric phenomena couple thermal fields to charge transport. They include the Seebeck effect, through which a temperature gradient establishes a thermoelectric potential, and the Joule, Thomson and Peltier heat sources or sinks that accompany current transport [1-4]. Previous studies have focused primarily on semiconductors and functional thermoelectric materials with Seebeck coefficients of several hundred $\mu V\ K^{-1}$ [5,6]. By contrast, conventional metals such as aluminium, iron and titanium typically have Seebeck coefficients of only a few $\mu V\ K^{-1}$ [7,8], and their thermoelectric responses are therefore commonly neglected in manufacturing processes such as casting, heat treatment and machining.

The ultrahigh temperature gradients of AM call this assumption into question, where heat source is concentrated over micrometre-to-millimetre scales, generating temperature gradients of $\sim 10^5$–$10^8\ K\ m^{-1}$ in and around the melt pool [9-12], far exceeding those in most conventional thermal-processing operations. The current depends not only on Seebeck coefficient but also on electrical conductivity, properties of solid and liquid phases, and paths available to charge transport. A sufficiently large temperature gradient can therefore generate a strong local current even in a metal

with a small Seebeck coefficient. The heat generated by the current might, in turn, modify the temperature field that initially drives it.

Intrinsic thermoelectric currents have been incorporated into previous melt-pool models to evaluate the resulting Lorentz forces under applied magnetic fields [9,13-15]. More recently, the presumed presence of strong intrinsic thermoelectric currents has also served as a key physical premise for explaining magnetic-field-mediated pore suppression in AM melt pools [13]. To our knowledge, however, these currents have rarely been identified experimentally. Because both the thermoelectric current and the resulting Lorentz force are difficult to observe directly in the melt pool, numerical simulation is generally required to understand and control their dynamic evolution. Moreover, most researchers just evaluate the current density, without feeding the Joule, Thomson and Peltier heat terms back into the energy balance. This one-way treatment is reliable only when these heat terms are genuinely negligible. Most thermoelectric magnetohrodynamic (TEMHD) models used in this context have addressed specific aspects of the problem. Zhou et al. [14]omitted the contribution of thermoelectric effects to the current flux inside the melt pool; Pham et al. [17]introduced the Seebeck effect and calculated the effect of different magnetic field directions on the Lorentz force. Wang et al. [9]further incorporated the magnetic advection–diffusion equation to compute the induced magnetic field under their processing conditions and found that its impact on the actual multi-physics coupling was minor. However, despite the strong thermoelectric-current coupling present in laser additive manufacturing, none of these studies fed the Joule, Thomson, and Peltier heat terms back into the energy balance. Consequently, the feedback of these heat sources on the original thermal and flow fields remains unaccounted for. Moreover, most experimental evidence for thermoelectric currents in laser AM has been inferred indirectly from the Lorentz force's influence on melt-pool dynamic flow, while direct dynamic measurements of

the thermoelectric current itself are still lacking. Three questions therefore remain: does AM produce a measurable transient thermoelectric response; how large and spatially heterogeneous is the current-density; and do thermoelectric heat terms appreciably re-modify the temperature and current density? Answering these questions is essential for a quantitative understanding on physical metallurgy of AM itself and on its regulation by external fields such as magnetic and electric fields.

Here we investigate AlSi10Mg, a conventional alloy with a Seebeck coefficient of only ~2 μV K^{-1}. We measure transient potentials near the melt pool under representative AM conditions—laser powder bed fusion (LPBF) and laser directed energy deposition (LDED)—and perform coupled multiphysics simulations incorporating thermoelectric current and Joule, Thomson and Peltier heat terms. We identify strong, anisotropic thermoelectric current densities in AM of ~10^6–10^8 A m^{-2}, exceeding values reported for many thermoelectric systems (~10^4–10^6 A m^{-2}) [6]. The associated thermoelectric heat terms are comparable to radiative and convective heat losses from the melt-pool surface and feed back on both the thermal and electrical fields. An AM melt pool should therefore be viewed not simply as a thermal–fluid system but as a coupled thermal–electrical–fluid system. Finally, we discuss the significance of intrinsic thermoelectric current density for the physical metallurgy of AM and for control by external magnetic and electric fields.

Results and discussion

Transient potential response during laser melting

We developed a dual-probe in situ system to record the transient potential generated during laser scanning (Fig. 1a; Fig. S1; Methods). Two tungsten probes with tip diameters of ~5 μm contacted points A and B on an AlSi10Mg substrate under microscopic guidance. The potential difference

between the two points during laser scanning was divided by their separation a to obtain the mean potential gradient $\nabla\Phi$. Line AB was perpendicular to the laser scan path and separated from it by distance d (Fig. 1b). The probes were kept outside the melt pool to avoid melting and additional thermoelectric potentials generated by probe heating (Fig. S1c). Thus, the experiment captured the potential response at measurement points near the melt-pool periphery under heat-input scales representative of LPBF and LDED. Without laser irradiation, the potential-gradient noise ranges were approximately ±0.5 V m^{-1} and ±0.02 V m^{-1} for the LPBF and LDED parameter sets, respectively (Fig. 1c,d; Methods).

For LPBF, using a laser-spot diameter of 80 μm and a scan speed of 1,000 mm s^{-1}, the magnitude of the mean potential gradient, $|\nabla\Phi|$, increased rapidly as the laser approached the probes. The signal peaked when the laser was closest to the probes at $t \approx 0.7$ ms and then decreased during cooling (Fig. 1e). As the laser power increased from 100 W to 300 W, the peak $|\nabla\Phi|$ increased from ~3 V m^{-1} to ~11 V m^{-1}. We multiplied $|\nabla\Phi|$ by the electrical conductivity σ to obtain the mean current density between the measurement points; over 100–300 W, its peak was ~3×10^7–1.35×10^8 A m^{-2} (Fig. 1f). LDED, using a laser-spot diameter of 2 mm and a scan speed of 20 mm s^{-1}, exhibited the same basic response over a longer timescale. When the laser was closest to the probes at $t \approx 0.1$ s, the peak $|\nabla\Phi|$ was ~0.15–0.8 V m^{-1} at 500–1,000 W laser (Fig. 1g), corresponding to peak current densities of ~2×10^6–9×10^6 A m^{-2} (Fig. 1h). The smaller signal than in LPBF arose mainly from the larger characteristic thermal scale and lower temperature gradient.

Note that we further attempted to directly probe the electrical potential response inside the melt pool by inserting the probes in the melting track. Taking the LDED process as an example (Fig. S2), the measured peak $|\nabla\Phi|$ within the melt pool reaches ~8.3–9.6 V m^{-1} at laser powers of 500–

1,000 W, which is approximately one order of magnitude higher than the corresponding thermoelectric potential gradients near the melt-pool boundary (~0.15–0.8 V m^{-1}, Fig. 1g). However, under such conditions, the temperature increase of the tungsten probe itself introduces an additional thermoelectric voltage, and this probe-induced contribution is difficult to quantitatively identify and decouple from the intrinsic melt-pool potential. Therefore, the potential inside the melt pool should not be regarded as an accurate measurement.

The consistency of the two power series shows that the experiment did not merely detect an isolated peak: the thermoelectric signal increased with heat input and emerged on the timescale of the corresponding process. For both parameter sets, the numerical calculations reproduced the signal rise time, power dependence and order of magnitude of the peak. After the laser passed, the experimental signal decayed more slowly than the simulated signal (Fig. 1e–h), possibly because the simulation zone limited by computational load is smaller than the actual zone of substrate, whereas the greater thermal mass of actual substrate causes the heat dissipation and cooling rate to be slower than the numerical predictions. Nevertheless, independent experiments under both conditions showed that the potential response evolved synchronously with laser size and power and agreed quantitatively with the model. The experiments confirmed the transient thermoelectric response at the melt-pool periphery; the spatially resolved thermoelectric current-density field inside the melt pool was obtained from the computational model.

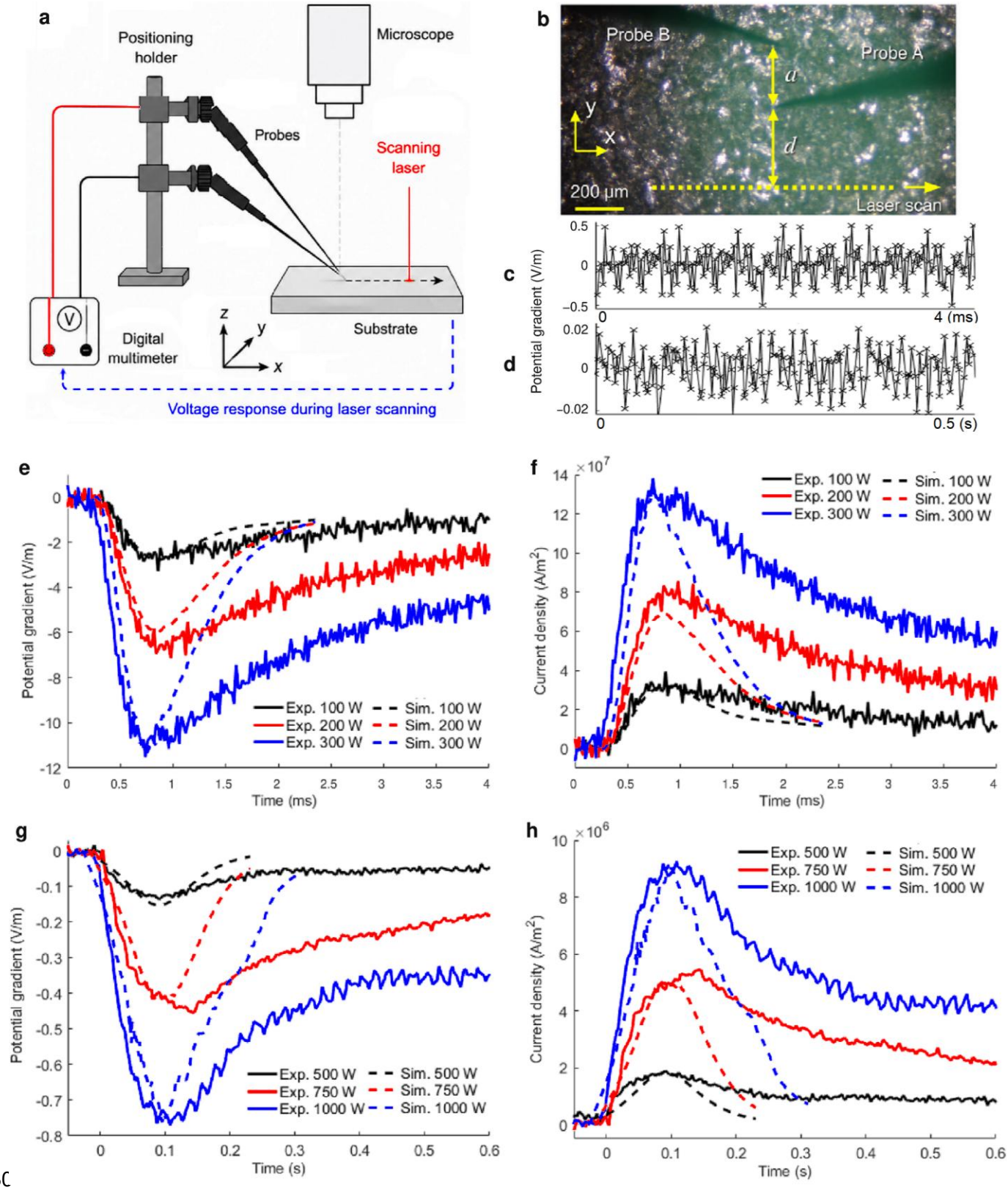

Fig. 1 Transient thermoelectric potential responses on two laser-melting scales. a, In situ dual-

tungsten-probe measurement system. **b,** Positions of the probes relative to the laser scan path. **c,d,** Noise ranges without laser irradiation for the LPBF (c) and LDED (d) parameter sets. **e,f,** Potential gradient $\nabla\Phi$ (e) and current density $\sigma|\nabla\Phi|$ (f) under different LPBF conditions; a = 30 μm, d = 80 μm, laser-spot diameter 80 μm, scan speed 1,000 mm s^{-1} and power 100–300 W. **g,h,** Corresponding LDED results; a = 0.5 mm, d = 2.5 mm, laser-spot diameter 2 mm, scan speed 20 mm s^{-1} and power 500–1,000 W. Solid and dashed lines denote experiment and simulation, respectively. See Methods and Supplementary Fig. S1.

Strong, heterogeneous thermoelectric current in melt pool

The model calculations show that, after the LPBF laser is switched on, the peak melt-pool temperature gradient rapidly reaches ~10^8 K m^{-1}, while the peak thermoelectric current density simultaneously reaches ~10^8 A m^{-2} and is distributed through the liquid melt pool and adjacent solid (Fig. 2a1–a2,b1–b2). At quasi-steady state (Fig. 2a3,b3), a keyhole forms on the laser-irradiated melt-pool surface, and the largest temperature gradients and current densities concentrate along the keyhole wall and extend downwards. Notably, although the temperature gradient at the solid–liquid interface and in the adjacent region of the melt pool is low—and hence so is the electric-potential gradient—a band of strong current density is present, mainly because the electrical conductivity increases abruptly from the liquid to the solid phase [18] (Supplementary Fig. S3). After the laser is switched off at t = 650 μs, the current density in the body of the melt pool decreases rapidly with the temperature gradient, whereas the strong-current-density band at the zone of solid–liquid interface persists briefly (Fig. 2a4–a5,b4–b5). Although the LDED melt pool has a different shape, it exhibits the same central feature: a strong and highly heterogeneous current-density field (Fig. 2c,d). In the laser-irradiated surface region, the peak temperature

gradient reaches ~10^6 K m^{-1} and the peak current density reaches ~10^7 A m^{-2}; high current densities are also present at the solid–liquid interface and in the adjacent exterior region. Moreover, because no deep keyhole forms under LDED conditions, the high surface current density does not extend down a keyhole wall as it does in LPBF.

Overall, thermoelectric current densities in the melt pool are of the order of 10^6–10^8 A m^{-2} and are highly heterogeneous. The laser-irradiated surface is one region of high current density due to the high temperature gradient and hence the high potential gradient. Additionally, high current densities are also present along the solid–liquid interface and around the melt-pool periphery because the electrical conductivity of the solid metal is substantially higher than that of the liquid. Our experiments measured the mean thermoelectric current density around the melt-pool periphery; together with the calculations, the results show that its magnitude is no substantially lower than that inside the melt pool.

The Seebeck coefficient of AlSi10Mg is one to two orders of magnitude lower than those of many thermoelectric materials, yet its melt-pool thermoelectric current densities in AM still reach 10^6–10^8 A m^{-2}, comparable to or greater than values of ~10^4–10^6 A m^{-2} in many high-Seebeck-coefficient thermoelectric systems[6]. This comparison does not imply that AlSi10Mg has a higher thermoelectric conversion efficiency; rather, it shows that extreme temperature gradients and the high electrical conductivity of metals can compensate for a small Seebeck coefficient in determining current density. Moreover, the principal concern in AM is the metallurgical behaviour of the metal, not efficient electrical-to-thermal energy conversion. The concentration of thermoelectric current density at the free surface and along the solid–liquid interface could potentially influence melt-pool evaporation and solidification.

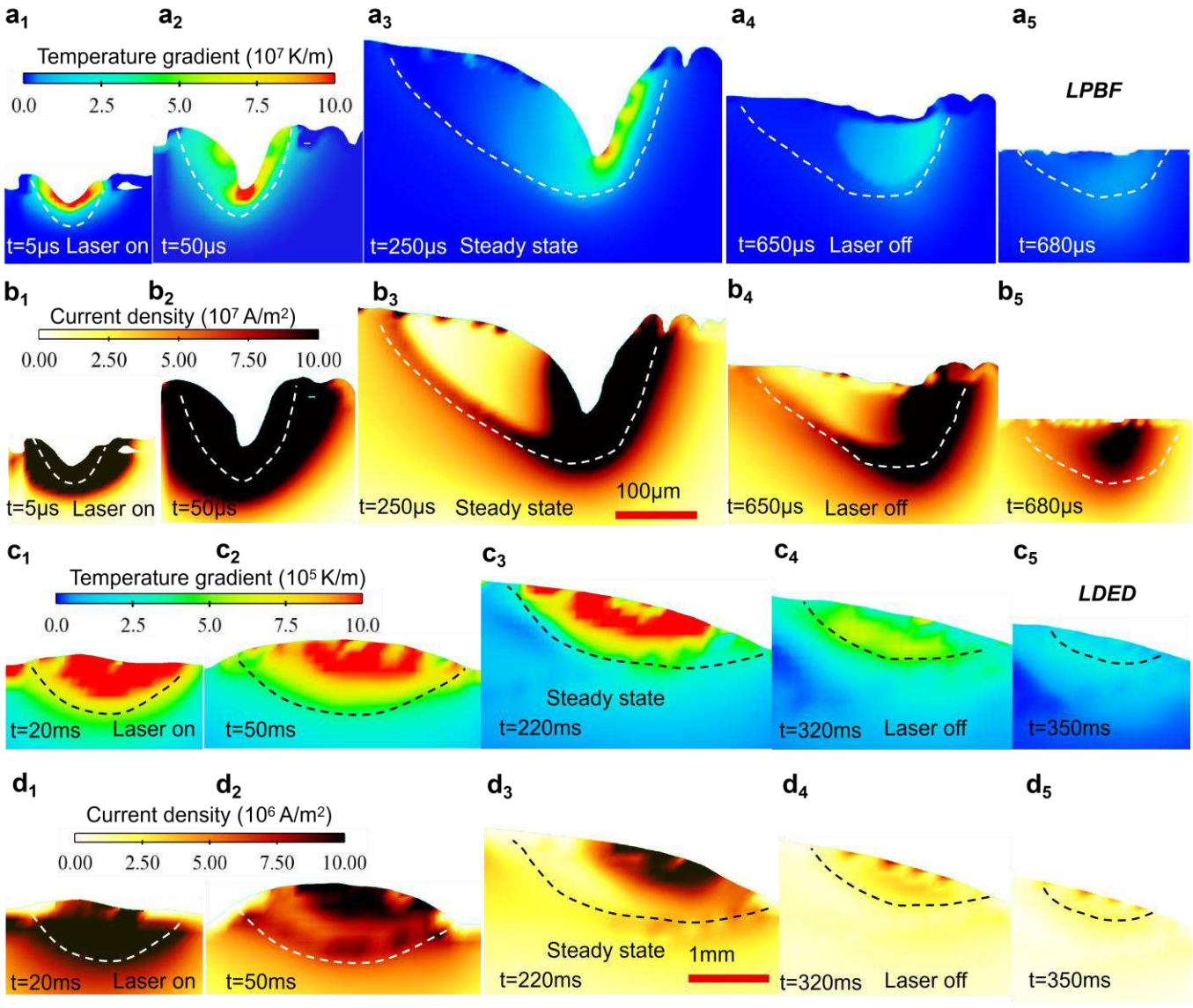

Fig. 2 Evolution of intrinsic thermoelectric current density across different process scales. **a,b,** Evolution of the temperature gradient (a1–a5) and current density (b1–b5) in LPBF melt pool; laser power 250 W, laser-spot diameter 80 μm and scan speed 1,000 mm s^{-1}, with the laser switched off at t = 650 μs. **c,d,** Corresponding LDED evolution; laser power 2,000 W, laser-spot diameter 2 mm and scan speed 20 mm s^{-1}, with the laser switched off at t = 320 ms. Dashed lines denote the solid–liquid interface of melt pool.

Anisotropy of thermoelectric current

Decomposing the current-density vector into the scan (X), transverse (Y) and vertical (Z) directions shows that it is not distributed uniformly through the melt pool (Fig. 3; Supplementary Videos S1 and S2(b,c,d)). In LPBF, the X and Y components have opposite directions on either side of the keyhole and converge towards the hottest region, whereas the Z component is concentrated mainly at the lower solidification front and extends upwards (Fig. 3a–c, Videos S1 (b,c,d)). LDED does not produce a deep keyhole, but its transverse components similarly converge from both sides towards the laser-heated region, and the vertical component extends from the lower interface to the upper surface (Fig. 3e–g, Videos S2 (b,c,d)). The Seebeck coefficient S of AlSi10Mg is negative; according to $J \approx -\sigma S \nabla T$, the principal current-density direction therefore tends towards the hot region (Fig. 3d,h, Supplementary Fig. S4). For a material with a positive Seebeck coefficient, the direction would be reversed.

The anisotropy of the melt-pool thermoelectric current-density field means that current-related thermal effects or other potential consequences are preferentially concentrated in specific regions and may differ in magnitude along the scan, transverse and build directions. This spatial organization also shows that a current density measured or estimated at a single point cannot represent the entire melt pool. Linking thermoelectric current density to melt-pool flow, thermal processes or solidification therefore requires both directional and spatial information.

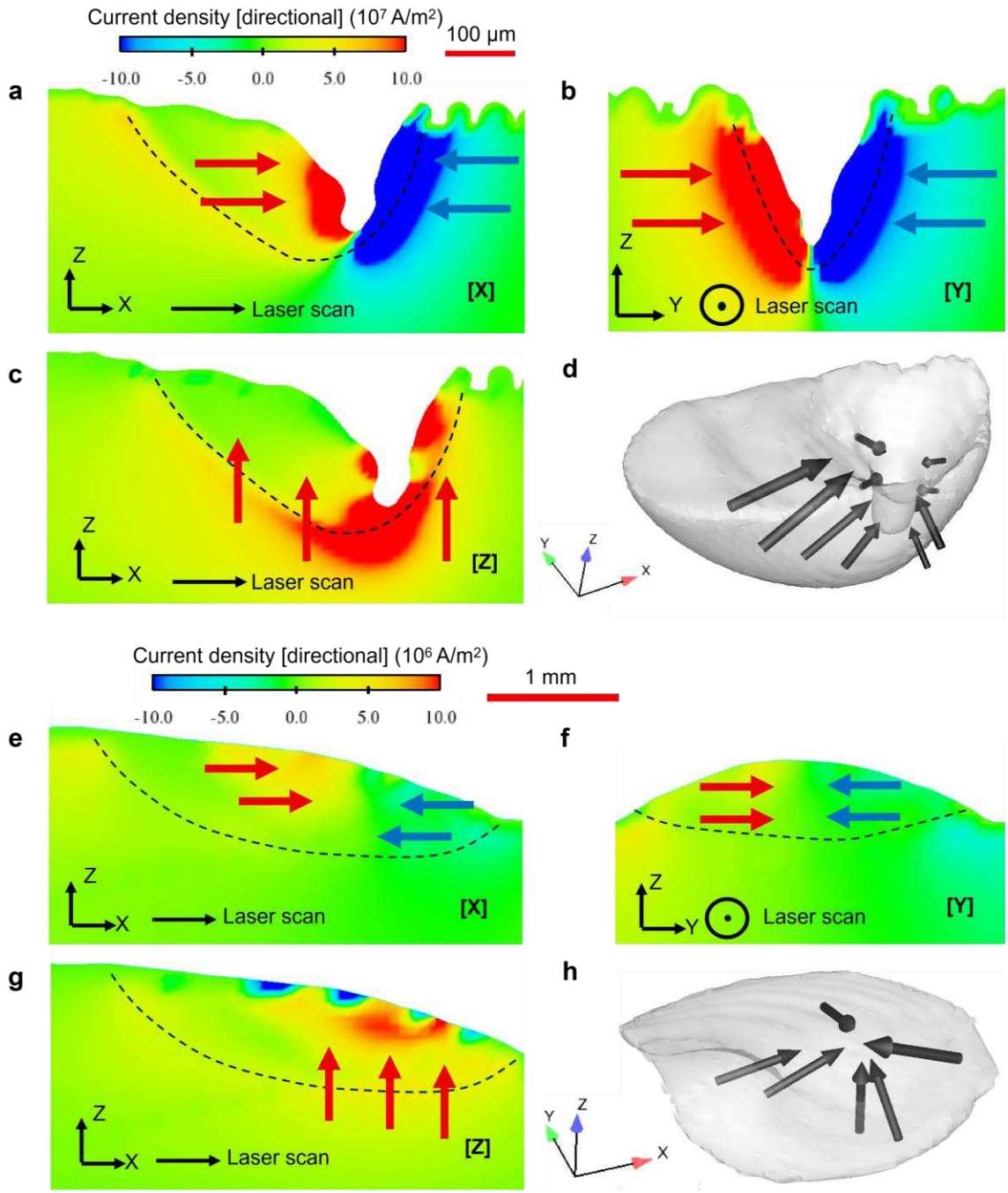

Fig. 3 Directionality and spatial heterogeneity of intrinsic thermoelectric current in melt pool. a–d, X (a), Y (b) and Z (c) components and resultant direction (d) of the LPBF current-density field. **e–h,** Corresponding LDED components (e–g) and resultant direction (h). Dashed lines denote the solid–liquid interface, and arrows indicate current direction; positive and negative values on the colour scale denote current components along and opposite to the indicated direction,

respectively. Dynamic results are provided in Supplementary Videos S1 and S2 (a,b,c,d).

Joule and Thomson heating comparable to melt-pool surface heat losses

Once the Seebeck current density is established, Joule heating Q_J, Thomson heating Q_T and Peltier heating Q_P all enter the energy balance. Joule heating arises from resistive dissipation (Eq.9), is always positive and is concentrated mainly in the high-current-density band within the laser-irradiated region (Fig. 4a2,c2; Supplementary Videos S1 and S2 (f)). The sign of Thomson heating (Eq. 10) is determined jointly by current direction, temperature gradient and $-(\mathrm{d}S/\mathrm{d}T)$. For AlSi10Mg, the Thomson term is predominantly exothermic in the high-temperature liquid zone, but endothermic near the solid–liquid interface zone (Fig. 4a1,c1, Videos S1 and S2 (e)). The Peltier term (Eq.11) is confined to the solid–liquid interface and, under the parameters considered here, provides very weak cooling (Fig. 4a3,c3, Videos S1 and S2 (g)). Whether the Thomson and Peltier effects produce heating or cooling depend on Seebeck coefficient $S(T)$ and its phase dependence (Detailed in Fig. S4), and should not be extrapolated directly to other materials.

We compare the thermoelectric heat terms with surface convective and radiative heat-loss terms within a single control volume on the fixed grid used for each process. For LPBF, the grid size is 5 μm: the local peaks of Joule and Thomson heating at the upper surface of melt pool are ~1.4×10^{-4} and ~1.2×10^{-4} W per control volume, respectively, and can exceed convective and radiative heat loss at the same discretization scale (Fig. 4b1). At the lower solid–liquid interface of the melt pool, Thomson cooling reaches approximately -9×10^{-5} W per control volume, whereas Joule heating is ~1.5×10^{-5} W per control volume (Fig. 4b2). For LDED, the grid size is 100 μm: the Joule and Thomson terms at the upper surface of melt pool are of the order of 10^{-5} W per control volume and can locally match the radiation term, whereas Thomson cooling remains dominant at

the lower solid–liquid interface of the melt pool (Fig. 4d1,d2). For both processes, the Peltier term is ~10^{-9} W per control volume, several orders of magnitude weaker than the other two terms and therefore nearly negligible (Fig. 4b2,d2).

Note that the magnitude of each heat term within a control volume depends on grid size and cannot be used directly to compare the fractions of total energy in LPBF and LDED. The robust conclusion follows from local comparisons on the same grid and at the same location: Joule and Thomson heating can equal or even exceed the surface heat-loss terms commonly retained in current melt-pool models. Our analysis does not challenge the established hierarchy of heat terms at the scale of the entire melt pool. Instead, it shows that thermoelectric heating and cooling introduce additional, highly localized and potentially important terms. Its contribution to the total energy may be not remarkable while still modifying a region that is small in scale but metallurgically important.

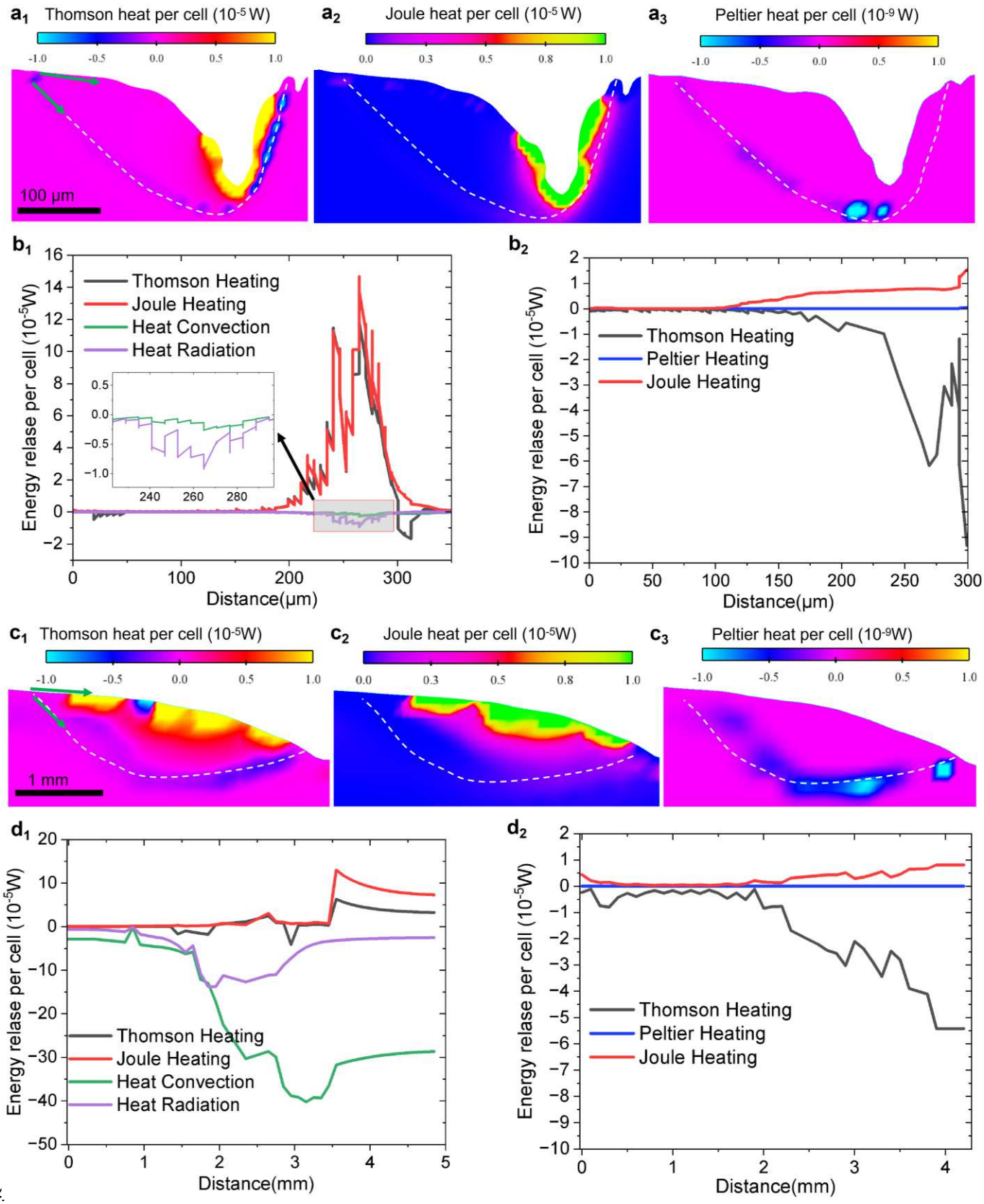
a1 Thomson heat per cell (10-5 W)
a2 Joule heat per cell (10-5 W)
a3 Peltier heat per cell (10-9 W)
100 μm
b1
Thomson Heating
Joule Heating
Heat Convection
Heat Radiation
Energy relase per cell (10-5W)
Distance(μm)
b2
Thomson Heating
Peltier Heating
Joule Heating
Energy relase per cell (10-5W)
Distance(μm)
c1 Thomson heat per cell (10-5W)
c2 Joule heat per cell (10-5W)
c3 Peltier heat per cell (10-9W)
1 mm
d1
Thomson Heating
Joule Heating
Heat Convection
Heat Radiation
Energy relase per cell (10-5W)
Distance(mm)
d2
Thomson Heating
Peltier Heating
Joule Heating
Energy relase per cell (10-5W)
Distance(mm)

244

Fig. 4 Joule, Thomson and Peltier heat terms associated with intrinsic thermoelectric current density. a,b, Spatial distributions of Thomson (a1), Joule (a2) and Peltier (a3) heat in LPBF, together with the thermoelectric heat terms and surface convective and radiative heat losses along the upper melt-pool surface (b1) and lower solid–liquid interface (b2); grid size 5 μm. **c,d,** Corresponding LDED distributions and line profiles; grid size 100 μm. Values denote power in each computational control volume and cannot be used to compare the total energy of different processes without accounting for grid size. Dashed lines denote the solid–liquid interface of melt pool. The origins of the horizontal axes in (b) and (d) correspond to the starting points of the green arrows in a1 and c1, respectively. Dynamic results are provided in Supplementary Videos S1 and S2 (e,f,g).

Bidirectional thermal–electrical feedback

In the fully coupled calculation, the temperature gradient drives the Seebeck current density, while the resulting heat terms feed back to modify both the temperature gradient and the current density, forming a quantifiable bidirectional feedback loop. To quantify this feedback, we divided the melt pool by isothermal surfaces from the solid–liquid interface at 830 K to the laser-irradiated upper surface and compared the fully coupled calculation with a control calculation in which Q_J, Q_T and Q_P were disabled (Fig. 5). In LPBF, the thermoelectric heat terms change the mean temperature gradient in each temperature region by ~2–10% and the corresponding mean current density by ~3–15% (Fig. 5a2–a3); in LDED, the respective changes are ~1–5% and ~2–5% (Fig. 5b2–b3). The deviations are the largest in the high-temperature-gradient and high-current-density regions near the upper surface of the melt pool.

These percentages should not be equated directly with a specific microstructural change, but they

act on the fundamental thermodynamic parameters that govern rapid solidification. The interfacial temperature gradient, solidification rate and their combinations influence interface morphology, cellular scale and solute redistribution. The thermal history at the upper surface of the melt pool also affects evaporation recoil pressure and keyhole stability. Thus, what we demonstrate directly is that the thermoelectric heat terms are sufficient to modify the thermal boundary conditions of these processes, not that thermoelectric current density has been shown to control a particular microstructure. More generally, future quantitative analyses of the peak magnitude and three-dimensional topology of intrinsic melt-pool current-density fields, and of the Lorentz forces, interface migration or other current-related effects that they might induce, should not merely post-process J on a prescribed temperature field. Such analyses should retain the feedback of the thermoelectric heat terms on the temperature gradient and current density, or first establish through a rigorous order-of-magnitude analysis that this feedback is negligible under the conditions considered.

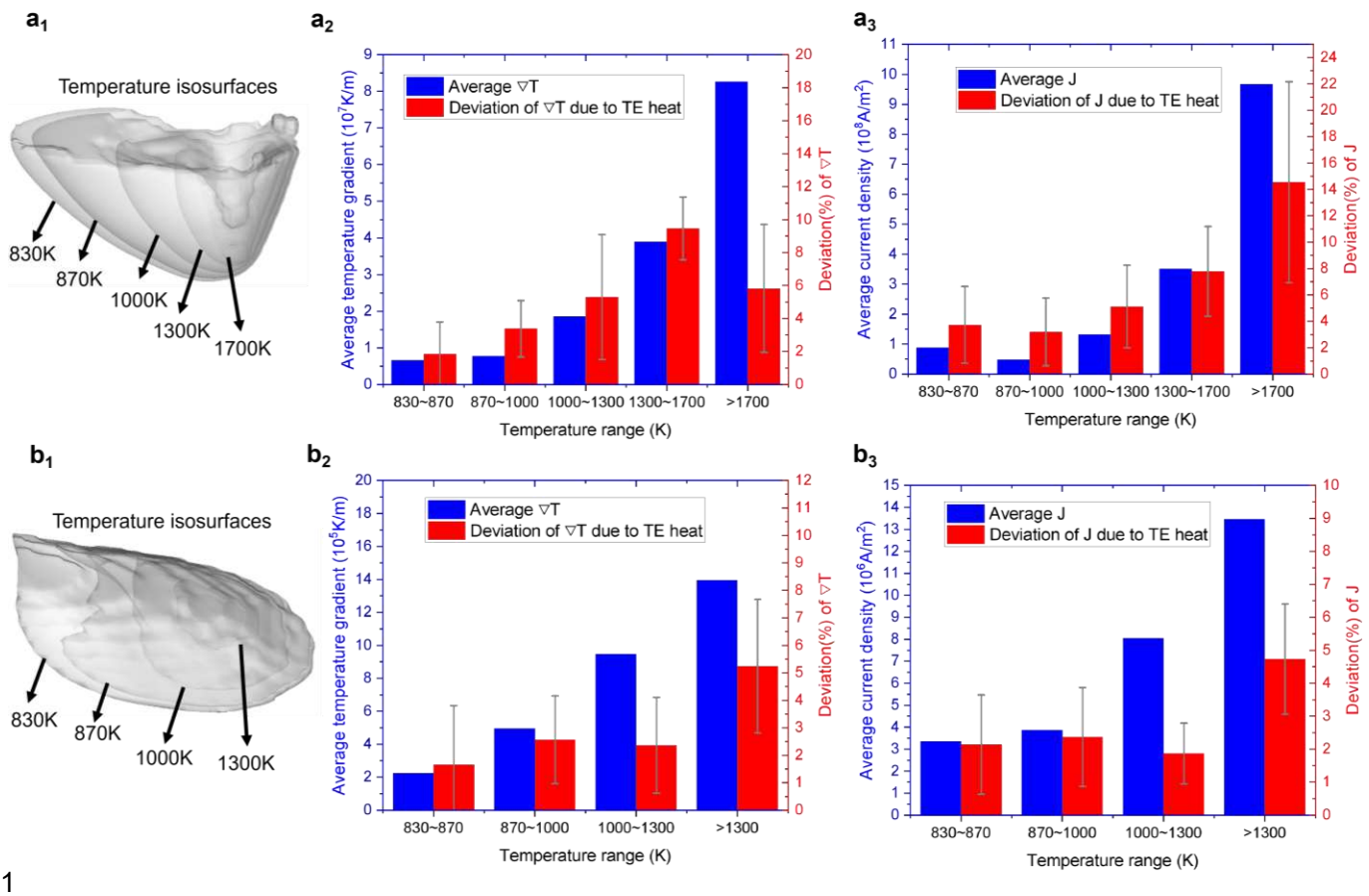

Fig. 5 Feedback of thermoelectric heat on the temperature gradient and current density. a, Isothermal partitioning of the LPBF melt pool (a1) and differences in the regional mean temperature gradient (a2) and mean current density (a3) between calculations with and without the thermoelectric heat terms. **b,** Corresponding LDED results. Bar heights denote means over five randomly selected time points. Values of deviations are means from five time points, with error bars indicating the minimum and maximum deviations.

Implications for physical metallurgy of AM and external-field control

Our results show that, under the extreme temperature gradients of AM, even a conventional metal with a small Seebeck coefficient, such as AlSi10Mg, can generate melt-pool thermoelectric current densities as high as ~10^6–10^8 A m^{-2}, with strongly heterogeneous magnitude and direction. The

melt pool should therefore be regarded not simply as a thermal–fluid system but as a coupled thermal–electrical–fluid system. Recognition of these high intrinsic melt-pool current densities could further advance our understanding of the physical metallurgy of AM.

First, the high current density itself could independently influence the metallurgical behaviour in AM. Studies of electrically assisted metallurgy have shown that sufficiently high current densities in an alloy (~10^4–10^6 A m^{-2}) can produce athermal electron-wind effects and additional electrothermal coupling, potentially modifying microstructural features such as dislocations[19-26]. The intrinsic thermoelectric current densities in AM melt pools clearly span the magnitudes required for these effects. However, it should be mentioned that, the duration, waveform and path of intrinsic AM currents differ from those of externally applied currents, so this comparison does not establish that any particular metallurgical effect occurs during melt-pool solidification. It does confirm an important prerequisite: high local current densities are already present in the melt pool and at the solidification interface. This electrical background can therefore be considered when investigating anomalous metallurgical behaviour with directional or interfacial characteristics.

Second, the Thomson and Joule heat terms associated with current densities of this magnitude can match convective and radiative heat losses from the melt-pool surface, providing additional, spatially asymmetric heat sources that feed back on the temperature and current-density distributions within the melt pool. We have not shown that these heat terms control a specific microstructure, but the results indicate that neglecting thermoelectric heating and cooling may yield an incomplete physical picture when establishing quantitative relationships between thermal history and metallurgical outcome. Moreover, feedback from the thermoelectric heat terms produces deviations in thermoelectric current density of up to ~15%, indicating that this factor cannot be entirely neglected in accurate analyses of electrically related AM behaviour and that

current theoretical models require corresponding refinement.

Finally, intrinsic thermoelectric current in melt-pool is particularly important for AM assisted by external magnetic[13,27-29] or electric fields[23-25]. We directly calculated a representative case with a transverse static magnetic field of 0.4 T (Fig. 6). For the alloy and LPBF/LDED conditions studied, the intrinsic thermoelectric current density was approximately one to two orders of magnitude greater than the motion-induced current density generated by melt-pool flow in the magnetic field((Fig. 6 a2 b2). This comparison does not imply the same ratio for every magnetic-field strength, orientation or material. It simply demonstrates that a strong current-density field is already present in the melt pool before a magnetic field is applied. Calculating magnetic forces only from the motion-induced current density would omit a larger current-density contribution, a point that has also been discussed in recent work [13]. In addition during the melting process, the variation in the induced current density and the associated electrical-related heat sources caused by the external magnetic field remain insignificant (Fig. 6 a3–a4,b3–b4).

We did not directly simulate an applied electric field and make only an order-of-magnitude assessment of electrically assisted processing. Previous current-assisted laser-processing studies have applied current through different electrode paths [23-25], with externally imposed current densities generally of the order of 10^4–10^5 A m^{-2} (Table S2). On the basis of our measurements and calculations (Fig. 1 and 2), the intrinsic thermoelectric current density in melt pool can be one to two orders of magnitude greater than these applied current densities. For each specific condition, the magnitudes and directions of the applied and intrinsic current-density fields should therefore be compared, and the effects of their superposition should be considered. In summary, interpreting either external field as acting on an initially current-free melt pool would omit the contribution generated by the thermoelectric current.

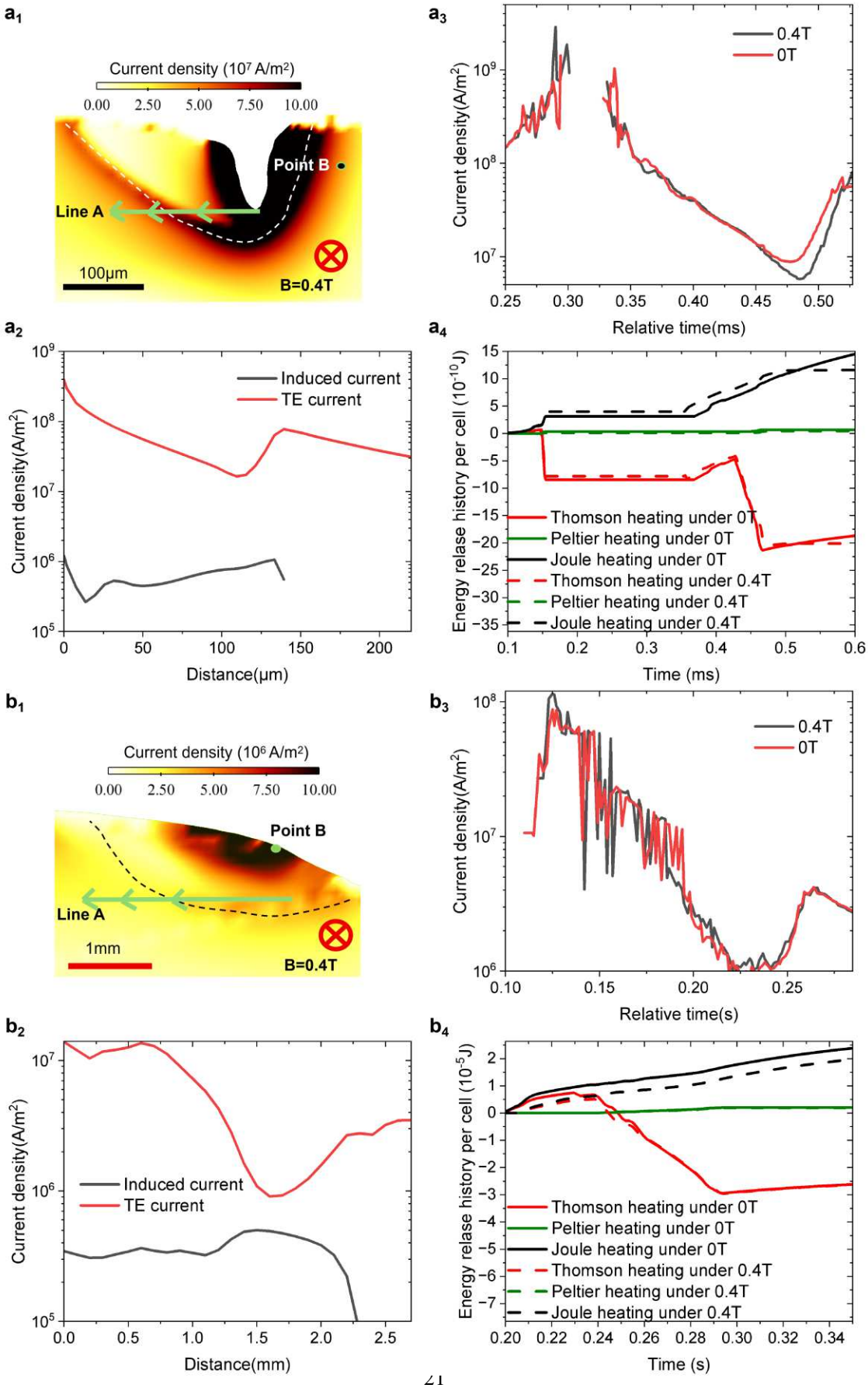
a1
Current density (10^7 A/m^2)
0.00 2.50 5.00 7.50 10.00
Point B
Line A
100μm
B=0.4T
a3
0.4T
0T
Current density(A/m^2)
Relative time(ms)
a2
Induced current
TE current
Current density(A/m^2)
Distance(μm)
a4
Energy relase history per cell (10^-10 J)
Thomson heating under 0T
Peltier heating under 0T
Joule heating under 0T
Thomson heating under 0.4T
Peltier heating under 0.4T
Joule heating under 0.4T
Time (ms)
b1
Current density (10^6 A/m^2)
0.00 2.50 5.00 7.50 10.00
Point B
Line A
1mm
B=0.4T
b3
0.4T
0T
Current density(A/m^2)
Relative time(s)
b2
Induced current
TE current
Current density(A/m^2)
Distance(mm)
b4
Energy relase history per cell (10^-5 J)
Thomson heating under 0T
Peltier heating under 0T
Joule heating under 0T
Thomson heating under 0.4T
Peltier heating under 0.4T
Joule heating under 0.4T
Time (s)

339

Fig. 6 **Intrinsic thermoelectric and motion-induced current densities under an applied magnetic field.** a, LPBF under a transverse magnetic field of 0.4 T: current-density field (a1), intrinsic thermoelectric and motion-induced current densities along the sampling line A (a2), and transient responses of current densities (a3) and thermoelectric heat terms (a4) at the sampling point B with and without the field. b, Corresponding results in LDED condition.

A cross-material, cross-process map of thermoelectric current

We compiled the electrical properties of the solid and liquid phases of Al, Ti, Cu, Ni and Fe near their melting points and used $J \approx \sigma S \nabla T$ to estimate current densities under temperature gradients of 10^4–10^9 K m^{-1} (Fig. 7; Table S3) [30-39]. This range encompasses representative temperature gradients in wire arc additive manufacturing (WAAM), LDED, electron-beam powder bed fusion (EB-PBF), LPBF and microscale LPBF (μ-LPBF). The estimated current densities span approximately 10^5–10^{11} A m^{-2}. At the same temperature gradient, Ti lies at the lower end and Ni at the upper end, while the current density in every metal increases approximately linearly with temperature gradient.

This map is intended for order-of-magnitude screening rather than prediction of the peak current in a specific melt pool. It does not fully account for temperature-dependent properties, alloy composition, phase-interface geometry, or the transient thermal history and morphology of the melt pool. When the simple estimate $\sigma|S||\nabla T|$ already exceeds a given magnitude, thermoelectric current density and the associated heat terms should not be excluded a priori solely because the metal has a small Seebeck coefficient. The magnitude map further indicates that this phenomenon is not confined to aluminium alloys or to a single AM process. The broad range across different metals also shows that a generic assumption based on the small Seebeck coefficients of metals is

insufficient. Differences in electrical conductivity and in solid- and liquid-phase properties can place two metals with similar Seebeck coefficients in different current-density ranges. Process-specific temperature gradients must therefore be evaluated together with material properties. The map provides a means of identifying, for a specific process and research objective, whether intrinsic thermoelectric current density needs to be considered.

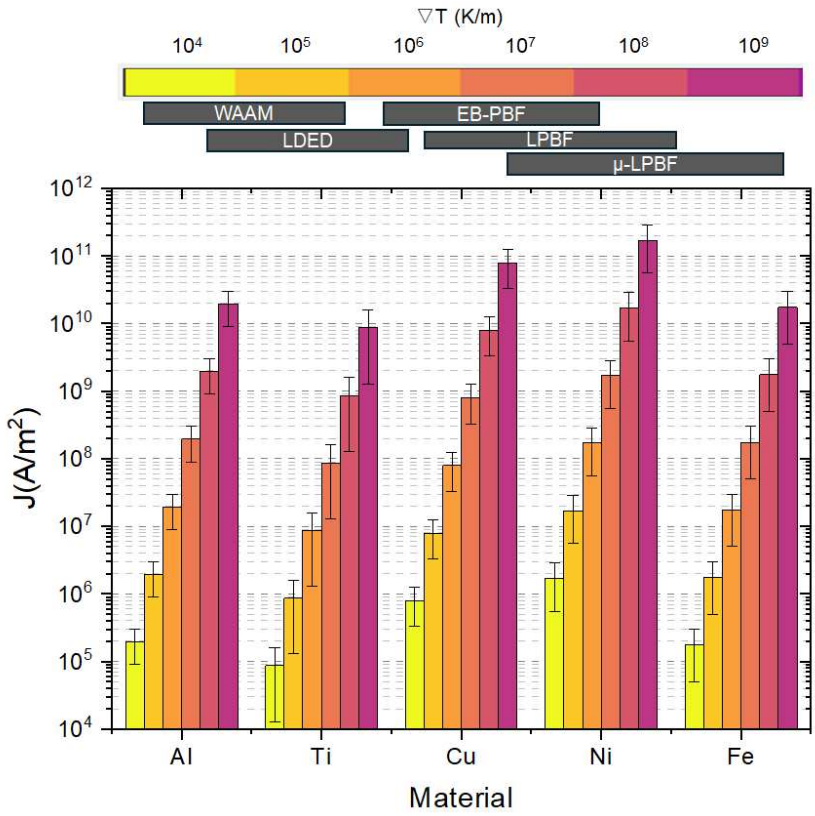

Fig. 7 Order-of-magnitude screening of current density in conventional metals under AM temperature gradients. Electrical properties of the solid and liquid phases of Al, Ti, Cu, Ni and Fe near their melting points are provided in Supplementary Table S3. The ranges above the plot denote representative temperature gradients for WAAM, LDED, EB-PBF, LPBF and μ-LPBF. Bar heights are estimated using $J \approx \sigma S \nabla T$; error bars indicate the range spanned by calculations using the material properties of the liquid and solid states. Note that the plot is intended for order-of-magnitude screening, not precise prediction of the peak current in a specific process.

Conclusion

By combining in situ transient-potential measurements with fully coupled thermal–electrical–magnetic–fluid simulations, we show that the extreme temperature gradients of laser AM generate intrinsic thermoelectric current densities of ~10^6–10^8 A m^{-2} in low-Seebeck coefficient alloy AlSi10Mg. These current densities are strongly anisotropic and spatially localized at the laser-irradiated melt-pool surface and around the solid–liquid interface. The associated Joule and Thomson heat terms can locally match or exceed convective and radiative heat losses from the melt-pool surface, whereas the Peltier term remains negligible; feeding all three terms back into the energy balance changes regional temperature gradients by ~1–10% and current densities by ~2–15%. The order-of-magnitude map further indicates that comparable or larger current densities can arise in AM of conventional structural metals when high electrical conductivity coincides with extreme temperature gradients. These results establish intrinsic thermoelectricity as a pre-existing and non-negligible component of the AM melt pool. Although the specific microstructural consequences remain to be demonstrated, quantitative assessments of metallurgical phenomena and magnetic- or electric-field-assisted processing in AM should account for the magnitude and direction of intrinsic thermoelectric currents and their associated thermal feedback, or rigorously establish the conditions under which these effects can be neglected. The model developed in this study provides an effective tool for studying magnetic-field-assisted laser additive manufacturing.

Methods

In situ measurement on transient-potential during laser melting process

Fig. 1 a–d illustrates the principle and workflow of the in situ thermoelectric-potential

measurements, and the experimental apparatus is shown in Supplementary Fig. S1. Laser melting was performed using an open-architecture laser AM system developed at the State Key Laboratory of Solidification Processing[40]. For the LPBF condition, the laser-spot diameter was 80 μm, the power was 100–300 W and the scan speed was 1,000 mm s^{-1}. For the LDED condition, the laser-spot diameter was 2 mm, the power was 500–1,000 W and the scan speed was 20 mm s^{-1}. AlSi10Mg was used as the substrate in both cases. Thermoelectric potential was measured with a high-precision digital multimeter (DM34461, Keysight Technologies, Inc.; sampling rate, 1 MS s^{-1}; basic DC-voltage accuracy, 30 ppm; maximum resolution, 7½ digits). The two probes connected to the multimeter were electrochemically machined tungsten probes, each 38.1 mm long, with a shaft diameter of 0.51 mm and a tip diameter of 5 μm. The actual contact area between a probe and the substrate surface was approximately circular, with a diameter of 5–10 μm. The probe-positioning stage had an X–Y–Z linear travel of 12 mm, an adjustable joint angle of 0–30° and a positioning accuracy of 5 μm. A microscope (XDS-10A, HAYZAR) with a maximum magnification of ×500 was mounted on the positioning stage to observe and verify the exact positions of the probe tips on the substrate. Each processing condition was tested three times. The potential difference between points A and B was recorded during laser scanning and divided by the separation between the two points to obtain the potential gradient. The thermoelectric current density was then obtained by multiplying the potential gradient by the electrical conductivity.

The potential data were acquired using number-of-power-line-cycles (NPLC) settings. Because the sampling-noise bandwidth under NPLC acquisition is affected by the required temporal resolution, a higher laser scan speed shortens the melt-pool lifetime, increases the required temporal resolution and consequently broadens the noise bandwidth. In addition, a shorter probe separation yields a smaller potential difference for a given potential gradient, increasing the

relative influence of measurement noise. In preliminary experiments, the probe separation, laser scan speed and NPLC value were therefore selected to maximize the number of data points acquired within the melt-pool lifetime while keeping the noise below 10% of the measured signal. During LPBF measurements, the minimum melt-pool lifetime near the measurement points was ~1 ms; NPLC was 0.001, the sampling interval was ~30 μs and the noise bandwidth was approximately ±0.5 V m^{-1}. During LDED measurements, the minimum melt-pool lifetime near the measurement points was ~0.3 s; NPLC was 0.1, the sampling interval was ~2.6 ms and the noise bandwidth was approximately ±0.02 V m^{-1}.

No powder was added in either the LPBF or LDED experiments because electrostatic forces caused powder to adhere to the probes, linking the two contact positions and producing a short circuit. As a tungsten probe immersed in the melt pool would heat rapidly and generate an additional thermoelectromotive force, the thermoelectromotive force measured inside the melt pool is just provided as qualitative evidence rather than an accurate quantitative measurement (Fig. S2).

Coupled thermal–electrical–fluid model with feedback from thermoelectric heat terms

In the melt-pool model, the liquid phase was assumed to be an incompressible Newtonian fluid in laminar flow. Melt-pool thermoelectric behaviour was calculated by coupling the laser heat input, Seebeck current density and thermoelectric heat terms. For cases with an applied magnetic field, models of the motion-induced current density and Lorentz force were also included.

Mass conservation equations:

$$\frac{\partial F}{\partial t}+\nabla\cdot(Fv)=0 \qquad (1)$$

$$\nabla\cdot(\rho v) = 0 \qquad (2)$$

where t is time, F is the fluid volume fraction, v is the fluid velocity and ρ is the fluid density.

Momentum conservation equation:

$$\frac{\partial \rho v}{\partial t}+\nabla\cdot(\rho v\otimes v)=-\nabla p+\mu\nabla^2 v+\left(\rho_T-\rho\right)g-\rho Dv+\frac{d\sigma}{dT}\left(\nabla T\, n(n\cdot\nabla T)\right)+P_{re}+F_{lz} \qquad (3)$$

In equation (3), $\left(\rho_T-\rho\right)g$ denotes the buoyancy force, ρDv the Darcy drag force [41], $\frac{d\sigma}{dT}\left(\nabla T\, n(n\cdot\nabla T)\right)$ the thermocapillary (surface-tension-gradient) force, $\frac{d\sigma}{dT}$ the temperature coefficient of surface tension and P_{re} the recoil pressure, which is calculated using the recently proposed evaporation model [10]in equation (4). Here, γ, F^- and G^- are dimensionless quantities related to the Mach number of the gas at the Knudsen layer, T_3 is the temperature at the Knudsen layer, and P_e and T_e are the alloy vapour pressure and evaporation temperature, respectively.

$$P_{re}=\frac{P_e e^{\gamma^2}}{2}\left(F^-+\sqrt{\frac{T_3}{T_e}}G^-\right)(2\gamma^2+1) \qquad (4)$$

In equation (3), F_{lz} denotes the Lorentz force, calculated using equation (5), where J is the current density determined from the electric-potential equation and B is the applied magnetic flux density.

$$F_{lz}=J\otimes B \qquad (5)$$

Energy conservation equation:

$$\frac{\partial(\rho I)}{\partial t}+\nabla\cdot(\rho v I)=\nabla\cdot(k\nabla T)+Q_{laser}+Q_{loss}+Q_J+Q_T+Q_P \qquad (6)$$

In equation (6), $I = C_pT+(1-F_S)L_m$ is the specific internal energy, where C_p and L_m are the specific heat capacity and specific latent heat of fusion, respectively. The laser heat input Q_{laser} follows a Gaussian distribution and is determined using equation (7), where P is the laser power, R_L is the laser radius and η is the laser absorptivity.

$$Q_{laser}=\frac{2\eta P}{\pi R_L^2}e^{\left(\frac{-2\left(x^2+y^2\right)}{R_L^2}\right)} \qquad (7)$$

In equation (6), Q_{loss} is the heat loss due to evaporation, calculated using the recently proposed evaporation model [10] in equation (8), where Lv is the latent heat of vaporization.

$$Q_{loss}=L_v\gamma\sqrt{\frac{2}{R}\frac{P_3}{T_3}} \quad (8)$$

The thermoelectric heat terms in equation (6) comprise Joule heating, Q_J, calculated using equation (9), where σ_c is the electrical conductivity; Thomson heating, Q_T, calculated using equation (10), where $T\frac{dS}{dT}$ is the Thomson coefficient; and Peltier heating, Q_P, calculated using equation (11), where S_s and S_l are the Seebeck coefficients of the solid and liquid phases, respectively, and ∇F_S is the solid-fraction gradient, normal to the solid–liquid interface and directed towards the solid.

$$Q_J=\frac{J^2}{\sigma_c} \quad (9)$$

$$Q_T=-T\frac{dS}{dT}J\cdot\nabla T \quad (10)$$

$$Q_P=-(S_s-S_l)TJ\cdot\nabla F_s \quad (11)$$

The thermal boundary condition includes convection and radiation, as given by equation (12), where h is the convective heat-transfer coefficient, 82 W m^{-1} K^{-1}; ϵ is the emissivity, 0.4; σ_s is the Stefan–Boltzmann constant, 5.67 × 10^{-8} W m^{-2} K^{-4}; and T_{env} = 300 K [9].

$$-k\nabla T\cdot n=\mathrm{h}(T-T_{env})+\epsilon\sigma_s(T^4-T_{env}^4) \quad (12)$$

Electric-potential and current-density equations:

$$\nabla^2\varphi=\nabla\cdot(-S\nabla T+v\otimes B) \quad (13)$$

$$J=\sigma_c(-\nabla\varphi+v\otimes B-S\nabla T) \quad (14)$$

The electric-potential distribution φ was obtained by solving the electric-potential equation (13), and the current-density distribution J was then determined using equation (14), where S is the Seebeck coefficient [7,8,42,43] and σ_c is the electrical conductivity [18].

Because the actual powder-bed dimensions are substantially larger than those of the computational

domain, Dirichlet boundary conditions with φ=0 were imposed on the substrate boundaries in the ±X, ±Y and −Z directions when solving the electric-potential equation. On the free surface defined by the volume-of-fluid method, a Neumann boundary condition was imposed by assuming a zero normal gradient of electric potential, that is, $\frac{\partial \varphi}{\partial n}$=0. Detailed physical properties are provided in Supplementary Table S1.

Data availability

The main data supporting the finding of this study are available within the article. Extra data are available from the corresponding author upon reasonable request.

Code availability

The TEMHD multi-physics coupling model based CFD solver is developed in Fortran to run the simulation. The codes that support the findings of this study are available upon reasonable request.

Acknowledgements

This work is supported by National Key Research and Development Program of China (Grant No. 2023YFB4604703), National Natural Science Foundation of China (Grant No. U22A20189) and A*STAR of Singapore under its Individual Research Project (M24N7c0082).

Author contributions

F.L.: Writing—review & editing, Writing—original draft, Visualization, Validation, Software, Methodology, Investigation, Formal analysis, Data curation, Conceptualization. H.C.: Writing—review & editing, Writing—original draft, Methodology, Validation, Investigation, Formal analysis. Y.S.: Writing—review & editing, Investigation, Data curation. H.Y.: Writing—review

& editing, Visualization, Formal analysis. M.W.: Writing—review & editing, Visualization, Formal analysis. W.Y.: Writing—review & editing, Visualization, Formal analysis, Conceptualization, Validation. X.L.: Writing—review & editing, Supervision, Resources, Project administration, Funding acquisition.

Competing interests

The authors declare no competing interests.

References

1 Jouhara, H. *et al.* Thermoelectric generator (TEG) technologies and applications. *International Journal of Thermofluids* **9**, 100063 (2021). https://doi.org/https://doi.org/10.1016/j.ijft.2021.100063

2 Winterbone, D. E. & Turan, A. in *Advanced Thermodynamics for Engineers (Second Edition)* (eds Desmond E. Winterbone & Ali Turan) 467–495 (Butterworth-Heinemann, 2015).

3 Lee, H. The Thomson effect and the ideal equation on thermoelectric coolers. *Energy* **56**, 61–69 (2013). https://doi.org/https://doi.org/10.1016/j.energy.2013.04.049

4 Chen, W.-H., Liao, C.-Y. & Hung, C.-I. A numerical study on the performance of miniature thermoelectric cooler affected by Thomson effect. *Applied Energy* **89**, 464–473 (2012). https://doi.org/https://doi.org/10.1016/j.apenergy.2011.08.022

5 Sandoz-Rosado, E. J., Weinstein, S. J. & Stevens, R. J. On the Thomson effect in thermoelectric power devices. *International Journal of Thermal Sciences* **66**, 1–7 (2013). https://doi.org/https://doi.org/10.1016/j.ijthermalsci.2012.10.018

6 Maduabuchi, C. *et al.* Thomson effect and nonlinear performance of thermoelectric generator. *Heat and Mass Transfer* **58**, 967–980 (2022). https://doi.org/10.1007/s00231-021-03153-3

7 Gripshover, R. J., VanZytveld, J. B. & Bass, J. Thermopower of Pure Aluminum. *Physical Review* **163**, 598–603 (1967). https://doi.org/10.1103/PhysRev.163.598

8 Sklyarchuk, V. *et al.* Structure Sensitive Properties of Liquid Al–Si Alloys. *International Journal of Thermophysics* **30**, 1400–1410 (2009). https://doi.org/10.1007/s10765-009-0585-3

9 Wang, L. & Yan, W. Thermoelectric Magnetohydrodynamic Model for Laser-Based Metal Additive Manufacturing. *Physical Review Applied* **15**, 064051 (2021). https://doi.org/10.1103/PhysRevApplied.15.064051

10 Wang, L., Zhang, Y. & Yan, W. Evaporation Model for Keyhole Dynamics During Additive Manufacturing of Metal. *Physical Review Applied* **14**, 064039 (2020). https://doi.org/10.1103/PhysRevApplied.14.064039

11 Yu, T. & Zhao, J. Quantifying the mechanisms of keyhole pore evolutions and the role of metal-vapor condensation in laser powder bed fusion. *Additive Manufacturing* **72**, 103642 (2023). https://doi.org/https://doi.org/10.1016/j.addma.2023.103642

12 Zhao, C. *et al.* Critical instability at moving keyhole tip generates porosity in laser melting. *Science* **370**, 1080–1086 (2020). https://doi.org/doi:10.1126/science.abd1587

13 Fan, X. *et al.* Magnetic modulation of keyhole instability during laser welding and additive manufacturing. *Science* **387**, 864–869 (2025). https://doi.org/10.1126/science.ado8554

14 Zhou, Y. *et al.* Thermo-fluid flow behavior of the IN718 molten pool in the laser directed energy deposition process under magnetic field. *Rapid Prototyping Journal* **29**, 460–473 (2023). https://doi.org/10.1108/RPJ-05-2022-0143

15 Lange, A., Cramer, A. & Beyer, E. Thermoelectric currents in laser induced melts pools. *Journal of Laser Applications* **21**, 82–87 (2009). https://doi.org/10.2351/1.3120213

16 Peng, G. *et al.* Ductilizing additively manufactured paramagnetic alloys via auxiliary magnetic field: Beyond the porosity effect. *International Journal of Machine Tools and Manufacture* **220**, 104422 (2026). https://doi.org/https://doi.org/10.1016/j.ijmachtools.2026.104422

17 Pham, D.-P. *et al.* Lorentz-force alignment governs keyhole stability in laser metal melting. *International Journal of Mechanical Sciences* **325**, 111877 (2026). https://doi.org/https://doi.org/10.1016/j.ijmecsci.2026.111877

18 Brandt, R. & Neuer, G. Electrical Resistivity and Thermal Conductivity of Pure Aluminum and Aluminum Alloys up to and above the Melting Temperature. *International Journal of Thermophysics* **28**, 1429–1446 (2007). https://doi.org/10.1007/s10765-006-0144-0

19 Zhou, C., Zhan, L., Liu, C. & Huang, M. Insights into electron wind force by a helical dislocation reconfiguration. *iScience* **26**, 106870 (2023). https://doi.org/https://doi.org/10.1016/j.isci.2023.106870

20 Xie, L., Sun, H., Wen, Y., Hua, L. & Zhang, L.-C. Electromagnetic treatment enhancing performance of metal materials: A review. *Progress in Materials Science* **153**, 101488 (2025). https://doi.org/https://doi.org/10.1016/j.pmatsci.2025.101488

21 Ashi, L., Xie, Z., Sun, H., Wang, J. & Huang, K. Effect of electromagnetic coupling treatment on the residual stress relief and mechanical properties of 7050 aluminum alloy. *Journal of Materials Science* **58**, 12097–12117 (2023). https://doi.org/10.1007/s10853-023-08775-y

22 Zhong, F. *et al.* Residual stress reductions of carbide cutting tools through applying pulsed magnetic field and coupled electromagnetic field – mechanism analysis and comparison study. *The International Journal of Advanced Manufacturing Technology* **121**, 4757–4775 (2022). https://doi.org/10.1007/s00170-022-09434-3

23 Zhai, L., Wang, Q., Zhang, J. & Ban, C. Effect of alternating current electric field on microstructure and properties of laser cladding Ni–Cr–B–Si coating. *Ceramics International* **45**, 16873–16879 (2019). https://doi.org/https://doi.org/10.1016/j.ceramint.2019.05.230

24 Wang, D., Zhu, Y., Qu, G. & Zhou, X. Research on Dilution of Laser Cladding Assisted by Pulsed Current Based on Orthogonal Experiment. *Journal of Physics: Conference Series* **1965**, 012087 (2021). https://doi.org/10.1088/1742-6596/1965/1/012087

25 Li, X. *et al.* Microscopic characteristics and properties of co-based coating by pulse current-assisted laser cladding on high carbon steel. *Surface and Coatings Technology* **494**, 131367 (2024). https://doi.org/https://doi.org/10.1016/j.surfcoat.2024.131367

26 Hou, M. *et al.* Effects of Pulsed Magnetic Fields of Different Intensities on Dislocation Density, Residual Stress, and Hardness of Cr4Mo4V Steel. *Crystals* **10**, 115 (2020).

27 Liu, F. *et al.* Effect of magnetic field orientation on suppressing porosity in steady-magnetic-field-assisted aluminum alloy deep-penetration laser welding. *Journal of Materials Processing Technology* **304**, 117569 (2022). https://doi.org/https://doi.org/10.1016/j.jmatprotec.2022.117569

28 Meng, X., Bachmann, M., Artinov, A. & Rethmeier, M. A study of the magnetohydrodynamic effect on keyhole dynamics and defect mitigation in laser beam welding. *Journal of Materials Processing Technology* **307**, 117636 (2022). https://doi.org/https://doi.org/10.1016/j.jmatprotec.2022.117636

29 Li, X. *et al.* On the enhanced strength-ductility synergy of magnesium alloy fabricated by laser powder bed fusion with a static magnetic field. *Journal of Materials Science & Technology* **242**, 138–155 (2026). https://doi.org/https://doi.org/10.1016/j.jmst.2025.04.018

30 Seydel, U. & Fucke, W. Electrical resistivity of liquid Ti, V, Mo and W. *Journal of Physics F: Metal Physics* **10**, L203 (1980). https://doi.org/10.1088/0305-4608/10/8/001

31 Bel'skaya, E. A. An Experimental Investigation of the Electrical Resistivity of Titanium in the Temperature Range from 77 to 1600 K. *High Temperature* **43**, 546–553 (2005). https://doi.org/10.1007/s10740-005-0096-2

32 Ho, C. Y. *et al.* Electrical Resistivity of Ten Selected Binary Alloy Systems. *Journal of Physical and Chemical Reference Data* **12**, 183–322 (1983). https://doi.org/10.1063/1.555684

33 Marwaha, A. S. & Cusack, N. E. The absolute thermoelectric power of liquid metals. *Physics Letters* **22**, 556 (1966). https://doi.org/https://doi.org/10.1016/0031-9163(66)90650-0

34 MacInnes, W. M. & Huguenin, R. Thermoelectric power near magnetic critical points: Iron. *Physics Letters A* **44**, 51–52 (1973). https://doi.org/https://doi.org/10.1016/0375-9601(73)90956-0

35 Bretonnet, J.-L., Auchet, J. & Gasser, J.-G. Electrical transport properties of the liquid Al · Cu alloys. *Journal of Non-Crystalline Solids* **117-118**, 395 – 398 (1990). https://doi.org/https://doi.org/10.1016/0022-3093(90)90961-K

36 Abadlia, L., Gasser, F., Khalouk, K., Mayoufi, M. & Gasser, J. G. New experimental methodology, setup and LabView program for accurate absolute thermoelectric power and electrical resistivity measurements between 25 and 1600 K: Application to pure copper, platinum, tungsten, and nickel at very high temperatures. *Review of Scientific Instruments* **85** (2014). https://doi.org/10.1063/1.4896046

37 Carreon, H., San Martin, D., Caballero, F. G. & Panin, V. E. The effect of thermal aging on the strength and the thermoelectric power of the Ti-6Al-4V alloy. *Physical Mesomechanics* **20**, 447–456 (2017). https://doi.org/10.1134/S1029959917040105

38 Worner, H. W. Thermoelectric Properties of Titanium with Special Reference to the Allotropic Transformation. *Australian Journal of Scientific Research Series A: Physical Sciences* **4**, 62–83 (1951). https://doi.org/10.1071/CH9510062

39 Roberts, R. B. The absolute scale of thermoelectricity II. *Philosophical Magazine B* **43**, 1125–1135 (1981). https://doi.org/10.1080/01418638108222579

40 Han, J. *et al.* Non-contact ultrasound to assist laser additive manufacturing. *Nature Communications* **16**, 7613 (2025). https://doi.org/10.1038/s41467-025-62803-w

41 Wang, L., Zhang, Y., Chia, H. Y. & Yan, W. Mechanism of keyhole pore formation in metal additive manufacturing. *npj Computational Materials* **8**, 22 (2022). https://doi.org/10.1038/s41524-022-00699-6

42 Shercliff, J. Thermoelectric magnetohydrodynamics. *Journal of fluid mechanics* **91**, 231–251 (1979).

43 Callen, H. B. The application of Onsager's reciprocal relations to thermoelectric, thermomagnetic, and galvanomagnetic effects. *Physical Review* **73**, 1349 (1948).

Supplementary Files

This is a list of supplementary files associated with this preprint. Click to download.

- SupplementaryMaterials.docx